Observation of void nucleation growth and coalescence in a model metal matrix composite using x-ray tomography

Arnaud Weck, David Wilkinson, E Maire

May 13, 2008

A. Weck
McMaster University, Department of Materials Science and Engineering. 1280 Main Street West, Hamilton, ON, Canada. weckag@mcmaster.ca
D. Wilkinson
McMaster University, Department of Materials Science and Engineering. 1280 Main Street West, Hamilton, ON, Canada.
E. Maire
MATEIS INSA-Lyon, F-69621, France UMR CNRS 5510.

Abstract

A model material with a core/shell design has been fabricated. The core consists of 50 μm diameter ZrO_2/SiO_2 particles in a pure aluminum matrix (99.9%) while the shell consists of particle-free aluminum. Such a design allows the sample to deform in a controlled manner. Void nucleation, growth and coalescence were precisely captured via in-situ tensile tests coupled with x-ray tomography. Samples with various volume fraction of particles in their core and various notch sizes have been tested. We show that the higher the volume fraction of particles and stress triaxiality, the lower the nucleation and coalescence strains. Depending on the interactions between voids and neck geometry, void growth occurs either mainly in the tensile direction or through the formation of a diamond-like shape. Finite element simulations and slip line fields demonstrate that the shape of the voids is a result of plasticity and neck geometry. Finally, a modified version of the Brown and Embury model for coalescence is developed to take into account the lower coalescence strains at high stress triaxialities.

1 Introduction

Ductile fracture of commercial purity metals involves a sequence of overlapping processes that includes the nucleation, growth and coalescence of voids. The main parameters affecting coalescence include: (a) the geometry (void size, shape, orientation, spacing) (b) the material properties (work hardening rate) and (c) the stress state (stress triaxiality) [1, 2, 3, 4, 5, 6, 7]. The experimental challenge is to experimentally vary these parameters in a controlled manner to evaluate their respective influences. Commercially available materials have complicated microstructure (random size, shape and distribution of inhomogeneities for example) which is difficult to analyze and they generally fail in a stochastic manner. This makes it difficult to capture the various stages of ductile fracture, especially the coalescence event and one needs to use instead model materials with controlled microstructure. Attempts to fabricate such model materials for the study of the ductile fracture processes have already been made. Babout et al. [8] and Gammage et al.[4] for example fabricated metal matrix composites made of an aluminum matrix reinforced by zirconia and alumina spheres respectively. These model materials are useful to study damage nucleation events but are of limited value when one wants to study the coalescence event in detail, because the sample still breaks in a stochastic manner.

In this work, in order to better control failure, a

metal matrix model material with a core/shell design (Figure 1(a)) has been fabricated and tested in situ in an x-ray tomography set-up. The effect of particle volume fraction (between 2% and 20%) and stress triaxiality (between 0.33 and 1.43) is investigated and the results are compared to the original and to a modified version of the Brown and Embury model [16] for void coalescence.

2 Experimental methods

2.1 Material fabrication

The composite material is made of zirconia/silica particles in a commercial purity aluminum matrix. The commercial name of the particles is Zirblast, purchased from the company Saint-Gobain Zirpro. They are made of ∼65% ZrO_2, ∼30% SiO_2 and ∼5% Al_2O_3. The particle powder is sieved between mesh sizes of 53 μm and 45 μm to obtain a narrow size distribution and thus reduce the particle size effect on the damage in the material. Once the powder is sieved, its size distribution is measured using a Horiba CAPA700 particle size analyzer that measures particle size distribution by liquid phase sedimentation. An average of 3 sets of measurements gives a mean particle diameter of 49.5 μm. Figure 1(b) shows an SEM image of the Zirblast powder, demonstrating the homogeneous particle size and its almost spherical shape.

The matrix is made from an atomized commercial purity aluminum powder. The aluminum powder has a purity of 99.9% and a mesh size -325 (equivalent to less than 44 μm). The same experimental procedure as described above is used to determine the mean particle diameter which is found to be 16 μm.

The composite has a core/shell design to prevent the material from failing too rapidly. The core is made of the composite mixture (zirconia particles + aluminum powder) and the shell contains only aluminum powder (Figure 1(a)).

The fabrication of the model material is done following a typical powder metallurgy route. The aluminum and zirconia powders are first mixed in order to obtain a homogeneous distribution of both powders. In a cold press, the mixture is poured into a hollow cylinder made of the aluminum powder to obtain the core/shell configuration. The whole is then cold pressed to a pressure of 35 MPa and hot pressed at 525°C under 75 MPa. The sintered sample is then extruded at 500°C at a speed of 1 to 2 mm/s. The extrusion ratio of 16:1 has been found to be sufficient to break the oxide layer on the aluminum powder and produce good bonding [9]. The grain size in the core after extrusion was measured on the polished and anodized samples via optical microscopy. It is ∼8 μm in the transverse direction and ∼20 μm in the extrusion direction.

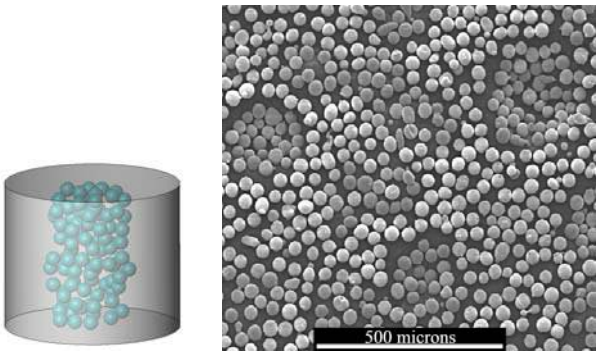

(a) (b)

Figure 1: (a) Schematic drawing of the composite material with the core/shell design. (b) SEM picture of the Zirblast powder after sieving between 53 μm and 45 μm.

The extruded material was machined in the form of dog-bone shaped samples. To study the effect of the number of particles on coalescence, particle volume fractions in the core of 2%, 5%, 10% and 20% were used. In some cases, notches of various radii R (2 mm, 0.5 mm and 0.25 mm) have also been machined in the middle of the sample gage length where the minimum sample diameter $2a$ is constant and equal to 2 mm. These notches resulted in triaxialities in the middle of the samples of 0.33, 0.55 and 1.43 respectively. These triaxialities were calculated using the following Bridgman expression [11]:

$$\frac{\sigma_m}{Y} = \frac{1}{3} + ln\left(\frac{a+2R}{2R}\right) \quad (1)$$

where σ_m is the mean stress and Y the yield stress. Because of the difficulty in obtaining the compostite core in the middle of the tensile samples, not all combinations of particle volume fraction and stress triaxiality were successfully tested in tomography.

2.2 Tensile testing in tomography

The samples were tested at the European Synchrotron Radiation Facility (ESRF) on beamline ID19. The energy used on this beamline was 30 keV and resulting voxel size used is 1.9 μm. Therefore, because of x-ray attenuation limitations, the samples have a gage length of 15 mm and a diameter of 2.5 mm. The experimental set-up is described in Buffière et al. [10].

Radiographs are recorded in real time during the tensile test to be able to visualize the material deformation while pulling on it. Void nucleation, growth and localization events can be observed on the radiographs as shown in Figure 2. The test can then be stopped whenever interesting features are observed on a radiograph and a tomograph can be acquired for 3D reconstruction (a tomograph consists of a series of radiographs taken at different angles).

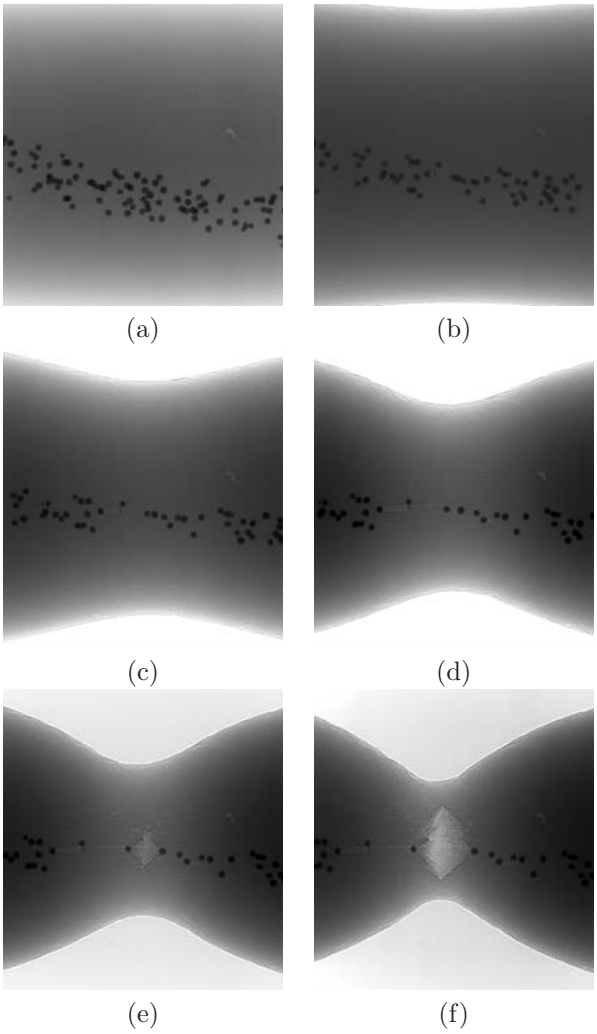

Figure 2: Sequence of radiographs from the composite sample containing 2% (J2) of particles taken at various engineering strains:(a) 0, (b) 0.204, (c) 0.237, (d) 0.258, (e) 0.271, (f) 0.280. The tensile direction is horizontal.

3 Tomography results

3.1 Void nucleation

The nucleation event is easily observed from the radiographs, as shown in Figure 3. The dominant nucleation mode is by decohesion of the particle-matrix interface at the poles of the particles. Nucleation occurs at the poles parallel to the direction of the applied load because this corresponds to the position of highest hydrostatic tension. Nucleation is preferred here over particle fracture because the soft aluminum matrix cannot transfer enough stress to the particle for them to break. The higher the volume fraction of particles in the core, the lower the nucleation strain (Figure 3).

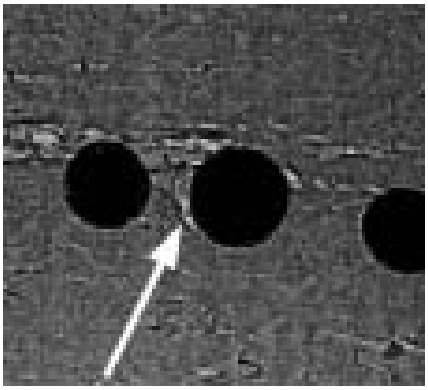

(a)

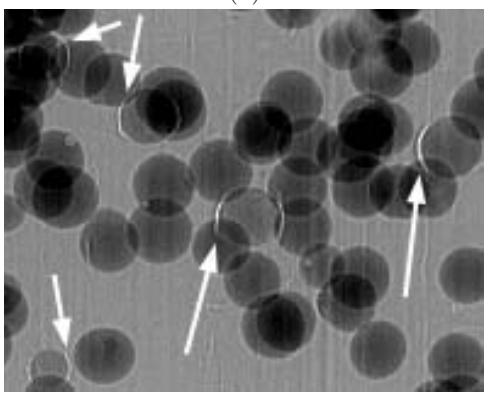

(b)

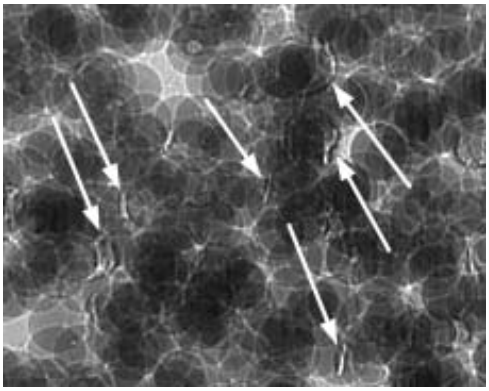

(c)

Figure 3: Radiographs taken at the onset of void nucleation for composite with volume fraction of particles (a) 2%, (b) 5% and (c) 10%. The nucleation engineering strains are respectively 0.2, 0.065, 0.037. The tensile direction is horizontal. The white arrows indicate the nucleated voids.

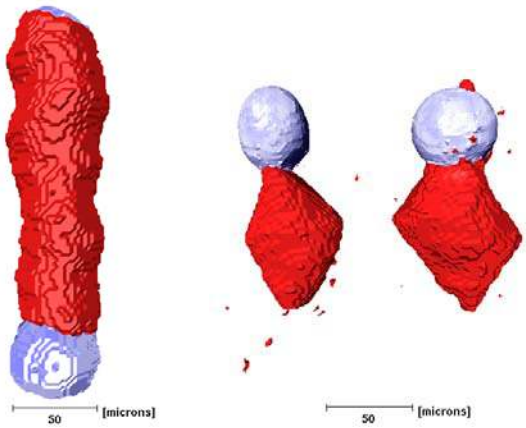

(a) (b)

Figure 4: Tomographic reconstruction of voids (dark colors) nucleated at Zirconia particles (light colors) when the deformation is (a) homogeneous and (b) localized.

3.2 Void growth

An interesting feature is the shape of the voids as they grow which is clearly shown in the tomographic reconstruction in Figure 4. The voids are cylinders when growing before coalescence (Figure 4(a)) while the shape of the voids after the coalescence is diamond-like as seen in Figure 4(b). It will be demonstrated in later sections that this diamond-like shape is a simple result of the plasticity and stress state in the sample.

3.3 Void Coalescence

The coalescence strain is chosen as that at which the holes start growing in the direction perpendicular to the direction of the applied load leading to the creation of a diamond-like cavity. To obtain precise results, the coalescence strains have been measured from the radiographs for which the sampling in strain is much higher. Figure 5 shows radiographs at the onset of coalescence in samples containing various volume fraction of particles in their core. Again, the coalescence strain decreases with increasing particle volume fraction in the composite core.

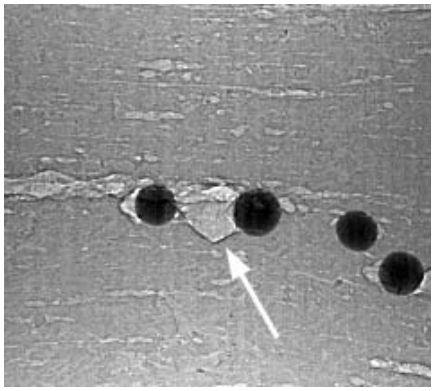

(a)

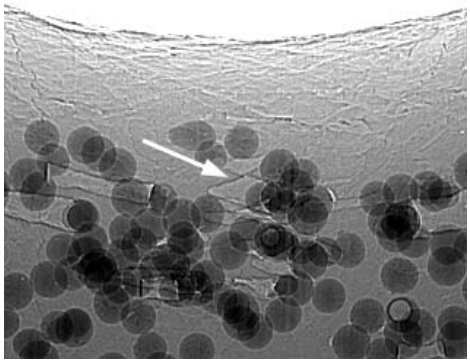

(b)

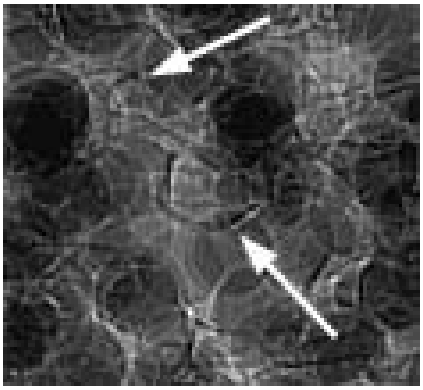

(c)

Figure 5: Radiographs taken at the onset of coalescence (when the voids start growing in the direction perpendicular to the direction of the applied load) for composites with volume fraction of particles equal to (a) 2%, (b) 5% and (c) 10%. The coalescence true strains are respectively 1.5, 1.1, 0.88. The tensile direction is horizontal. The white arrow indicates the coalescing void.

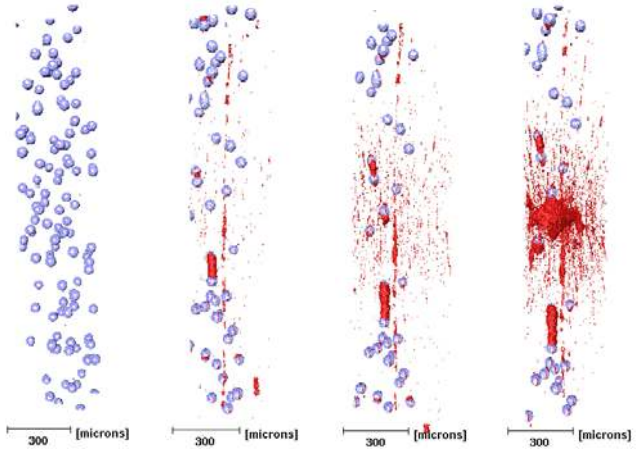

(a) (b) (c) (d)

Figure 6: Sequence of tomographic reconstructions showing the Zirconia-Silica particles (light colors) and the voids (dark colors) for the composite with core/shell design containing 2% of particles in its core (J2) and taken at various engineering strains: (a) 0.000, (b) 0.203, (c) 0.238, (d) 0.258. The tensile direction is vertical.

3.4 Entire ductile fracture process

The 3D reconstruction of the sample containing 2% particles in its core is shown in Figure 6 for various strains. As for the radiographs shown in Figure 2, the nucleation, growth and localization (or coalescence) events can be observed. However, collateral damage by void nucleation which occurs probably at the alumina particles can also be visualized in Figure 6(c-d). This secondary void nucleation mechanism was more difficult to observe in the radiographs of Figure 2.

4 Behavior of uniform samples

4.1 Fracture surfaces and strains

The fracture surfaces of the composite with core/shell design tested during tomography is shown in Figure 7. The corresponding strains to failure are shown

Table 1: Failure strains for composite material with core/shell design tested ex-situ.

Volume fraction of particles	2%	5%	10%	20%
Failure strains	2.57	2.34	1.64	2.34

in Table 1 and are calculated using

$$\varepsilon = 2\ln\left(\frac{D_0}{D}\right) \tag{2}$$

where D_0 and D are the initial and final smallest cross sectional diameters respectively. One can see that the failure strains are fairly independent of the volume fraction of particles. This is due to the controlling effect of the pure aluminum shell around the composite core. The low failure strain value in the 10% case is due to the higher proportion of composite core versus shell compared to the other sample as seen in Figure 7(c).

4.2 True stress-strain curves

A series of radiographs were taken at different strains for samples with volume fractions of 2%, 5% and 10% in their core (see Figures 2 for the 2% case). From the radiographs the smallest diameter in the neck can be measured and the associated minimal cross sectional area calculated. This is only valid if the cross section of the sample remains circular during deformation which is a good assumption considering the shape of the fracture surfaces shown in Figure 7. The true stress σ can then be calculated using:

$$\sigma = \left(\frac{F}{\pi a^2}\right) \tag{3}$$

where F is the load and a the radius of the smallest cross section in the neck. However, when a lot of damage accumulates in the sample as is the case in Figure 2(e) and (f), equation 3 leads to an unrealistic decrease in the true stress as shown in Figure 8(a) (labelled "Smallest diameter"). This problem can be solved by removing the voids from the calculated area and the resulting curve labelled "Smallest diameter without voids" is shown in Figure 8(a). Also, the calculated true stress is still only an averaged value of the stress over the whole cross section of the sample. When the sample starts to neck, the stress distribution in the neck is no longer uniform. In order to correct for the higher stress triaxialities found in the middle of the sample, Bridgman [11] proposed that the measured true stress σ_{meas} be corrected to the true stress σ_{cor} through the following equation:

$$\sigma_{cor} = \sigma_{meas}\left[\left(1+\frac{2R}{a}\right) ln\left(1+\frac{a}{2R}\right)\right]^{-1} \tag{4}$$

where R is the radius of curvature of the neck. The Bridgman equation has sense only while there is no significant damage in the sample. It can then only be applied up to the deformation shown in Figure 2(d) because in the cases shown in Figure 2(e) and (f) the internal crack leads to higher stress concentration at its tips and would require finite element analysis to solve for the stress state. The above procedure has been carried out for the various samples tested and the results are shown in Figure 8(b). The arrows labelled ε_c in Figure 8(b) represent the point at which coalescence starts. The failure strains measured from the SEM images of the fracture surfaces are shown by the arrows labelled ε_f in Figure 8(b).

5 Behavior of notched samples

Samples with a core/shell design and with pre-machined notches of various radii have been tested in tomography to study the effect of stress triaxiality defined as the mean stress over the equivalent stress (σ_m/σ_Y) on coalescence. The resulting stress triaxialities are 0.55, 1.03 and 1.43. All samples have the same initial minimum cross sectional area with a diameter of 2 mm. The coalescence strains were obtained from the radiographs as described earlier and the failure strains from SEM pictures of the fracture surfaces. Another definition of failure strain exists for notched samples where a diametrical extensometer is mounted across the minimum section of the sample. Failure is said to occur when a break appears in the load-diameter deformation curve. Such an approach is especially useful for samples failing by shear lips formation where the cross sectional area at fracture is difficult to quantify under an SEM. However,

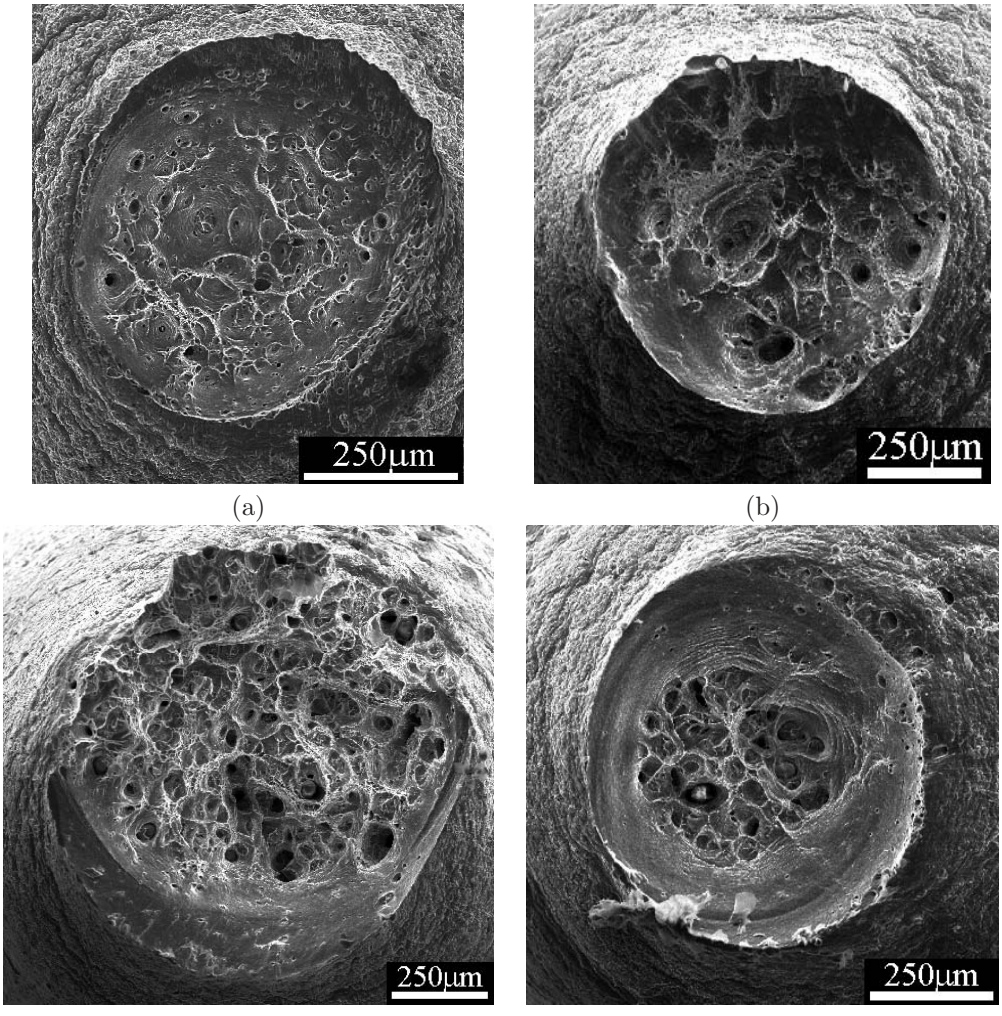

(a) (b)

(c) (d)

Figure 7: SEM image of the fracture surface of the composite samples with core/shell design tested in tomography with volume fraction of particles in the core of (a) 2% (J2), (b) 5% (C1), (c) 10% (E2) and (d) 20% (G1).

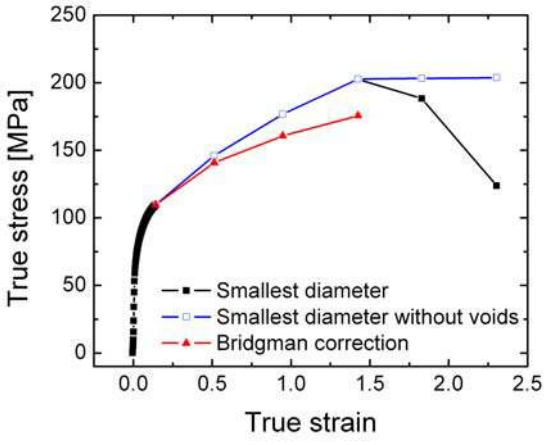

(a)

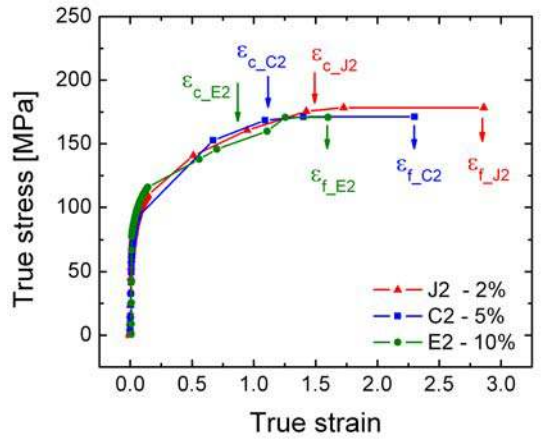

(b)

Figure 8: (a) Plot of the true stress versus true strain curves using equation 3 and using the Bridgman correction (equation 4) for a sample with a core/shell design containing 2% volume fraction of particles in its core. (b) Plot of the true stress versus true strain curves using the Bridgman correction (equations 4). The arrows placed above the curves point at the coalescence strain whereas those under are at the failure strain.

Table 2: Coalescence and failure strains for composite material with core/shell design and notches tested in-situ. The percentage reduction compared to samples without notches (Table 1) is calculated for both coalescence and failure strains.

Sample	JT3 (2%)	CT1 (5%)	CT2 (5%)	ET3 (10%)
Triaxiality	T=1.43	T=0.55	T=1.03	T=1.43
Coalescence strains	0.43	0.58	0.43	0.21
Reduction compared to uniform samples	71%	50%	60%	68%
Failure strains	2.27	2.00	1.76	1.46
Reduction compared to uniform samples	20%	13%	23%	8%

the samples tested in this study do not fail by shear lips formation but neck down to a line which enables precise measurements of the area at fracture. Furthermore, approaches using diametrical extensometers assume that the difference between the nucleation and failure strains can be neglected. This is not the case for very ductile samples as the ones shown in this manuscript where relatively large elongations are required to reach failure after void nucleation. Therefore, in this study, the failure strain of notched samples is calculated from SEM observations of the fracture surfaces. The results are shown in Table 2. One can see that the failure strains are not much different (about 15% lower) than that obtained for the samples without notches. This is again attributed to the shell which controls fracture. However, the coalescence strains are drastically reduced due to the presence of notches with a maximum reduction of about 70%. The reduction of the coalescence strains scales with the stress triaxiality in the sample. The higher the stress triaxiality, the lower the coalescence strain.

6 Comparison with Brown and Embury model

In the following, we present a comparison between experiments and the Brown and Embury model [16] for void coalescence. The Brown and Embury model is chosen for its simplicity which enables a better understanding of the parameters controlling void coa-

lescence. Indeed, in the following sections we show the strong effect of the stress triaxiality on the coalescence strains and propose a modified version of the Brown and Embury model to better predict the failure of notched samples.

6.1 Original Brown and Embury model

Brown and Embury [16] proposed a geometrical model for coalescence based on the void length and spacing. It stipulates that when the void length is equal to the intervoid spacing, shear bands at 45° can form and coalescence can occur as described by the following equation:

$$2R_1 = \lambda \tag{5}$$

where R_1 is the radius of the void in the tensile direction and λ the mean ligament length between the voids. In terms of strain, the main governing equation is formulated as follows:

$$\varepsilon_f = ln\left(\sqrt{\frac{\pi}{6V_f}} - \sqrt{\frac{2}{3}} + e_n\right) \tag{6}$$

where ε_f is the coalescence strain, V_f is the volume fraction of particles and e_n is the engineering nucleation strain. From the radiographs shown previously, the nucleation and coalescence strains can be precisely obtained (Figures 3 and 5). The experimental results are compared with the Brown and Embury model in Figure 9. When no Zirconia/Silica particles are present in the composite core, failure occurs at the aluminum oxide particles which are a result of the powder metallurgy fabrication route. The volume fraction of these oxides is estimated from the oxide layer present around the aluminum particles before the hot pressing and extrusion processes. An oxide layer of 10 nm is found to be a good estimate for an atomized aluminum powder as shown by Tang et al. [15]. Knowing that the average particle diameter found in section 2.1 is 16 μm, the average volume fraction of oxide is $1-(16-0.01)^3/16$ which is about 0.2%. The nucleation at the alumina particles is assumed not to be influenced by the presence of a few

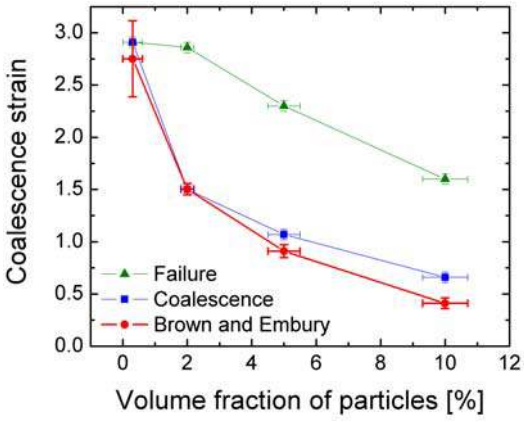

Figure 9: Comparison between the experimental coalescence strains and the predicted strains using the Brown and Embury model (equation 6).

Zirconia particles, and the nucleation strain is therefore taken from the composite sample with 2% of Zirconia particles. The engineering nucleation strain at the oxides is ∼0.25 as shown in Figure 6(c) where a significant amount of collateral damage is observed.

One can see that the Brown and Embury equation predicts the coalescence strains fairly well especially at low volume fractions. However, it cannot predict the coalescence strain of notched samples which are ∼70% lower than that of the uniform samples. This is why the model has been modified in the following section.

6.2 Modified Brown and Embury model

The Brown and Embury model states that coalescence occurs when the length of the ligament between the voids is equal the the length of the void. When the stress triaxiality is low, the length of the ligament does not vary significantly since the voids grow mainly in the tensile direction. However, when the stress triaxiality is high, the voids also grow in the direction perpendicular to the tensile direction. In that case, the length of the ligament between the voids will significantly decrease as the voids are growing, leading to an earlier failure of the sample. The new

model proposed here is the same as that of Brown and Embury in its definition but takes into account the lateral growth of the voids. The new coalescence condition is now as follows:

$$2R_1 = \lambda_s - 2R_3 \tag{7}$$

where R_1 is the radius of the void in the tensile direction, R_3 is the radius of the void in the direction perpendicular to the tensile direction and λ_s is the mean distance between the center of the voids defined as:

$$\lambda_s = R_0\sqrt{\frac{3}{2}}\sqrt{\frac{\pi}{V_f}} \tag{8}$$

The value of R_1 and R_3 are integrated from the Rice and Tracey equations [5]. For an initially spherical void in uniaxial tension this integration, proposed by Le Roy et al. [12], gives:

$$R_1 = R_0\ exp(D\varepsilon)\left[2\ exp\frac{3}{2}\varepsilon - 1\right]^{2/3} \tag{9}$$

$$R_3 = R_0\ exp(D\varepsilon)\left[2\ exp\frac{3}{2}\varepsilon - 1\right]^{-1/3} \tag{10}$$

where R_0 is the initial void radius taken as the particle radius (R_0=25 μm), ε the mean tensile strain and D is:

$$D = 0.56\ sinh\left(\frac{3\sigma_m}{2Y}\right) \tag{11}$$

σ_m/Y is the stress triaxiality. Equation 7 can be solved numerically and the result is the intersection of the curves for $2R_1$ and $\lambda_s - 2R_3$ plotted as a function of strain. The resulting coalescence strains are shown in Table 3. The results of the modified model give much better predictions when the triaxiality is increased. A parametric analysis has been done to study the effect of the triaxiality on the values of $2R_1$ and $\lambda_s - 2R_3$ and on the void volume fraction on the coalescence strain. Master curves can then be plotted as shown in Figure 10 to obtain the coalescence strain knowing the volume fraction of particles in the composite and knowing the applied stress triaxiality. One can see that at high stress triaxialities, the effect of the volume fraction of particles on the coalescence strain is much less than at low triaxialities. This is because the higher the stress triaxiality, the faster the holes grow toward each other and the lower the effect of the holes spacing.

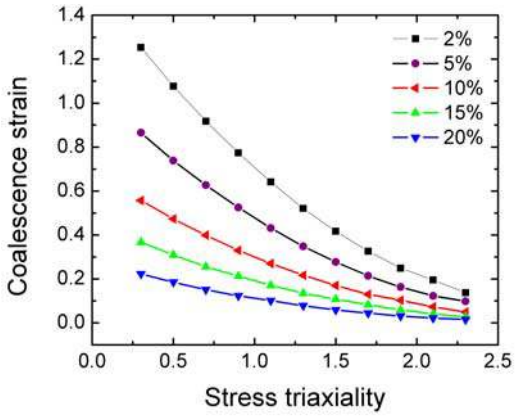

Figure 10: Master curves obtained from the modified Brown and Embury model showing the effect of the stress triaxiality and the void volume fraction on the coalescence strain.

Table 3: Comparison between the original Brown and Embury model and the modified model.

Material	Experiments	Brown and Embury model	Modified Model
A - 0.2% - T=0.33	2.91	2.75	2.16
J2 - 2%/1% - T=0.33	1.50	1.50/1.89	1.22/1.51
C2 - 5% - T=0.33	1.07	0.91	0.84
E2 - 10% - T=0.33	0.66	0.41	0.55
JT3 - 2% - T=1.43	0.43	1.47	0.45
CT1 - 5% - T=0.55	0.58	0.90	0.71
CT2 - 5% - T=1.03	0.43	0.90	0.46
ET3 - 10% - T=1.43	0.21	0.42	0.19

7 Discussion

7.1 Comments on the tomography technique

The onset of void coalescence is better captured using the radiographs because they are taken during the entire deformation of the sample at a fairly high rate

(∼500 radiographs per test). Tomograms are only acquired at a few given strain levels which will generally not be exactly at the coalescence strain. The radiographs are particularly useful when the volume fraction of particles is low. When too many particles are present, it becomes difficult to separate the coalescence events that are occurring through the volume as shown in Figure 5(c). In that case, the tomograms are more helpful. Furthermore, to obtain the real shape of the voids, it is necessary to look at the tomograms because the radiographs are only the projection of the 3D objects onto a 2D plane.

Therefore, to obtain precise information, radiographs are necessary to capture the onset of coalescence and tomographs are necessary to visualize the shape of the voids in 3D and to extract quantitative information such as void volume fraction, void geometry (major and minor diameter of the voids, etc.).

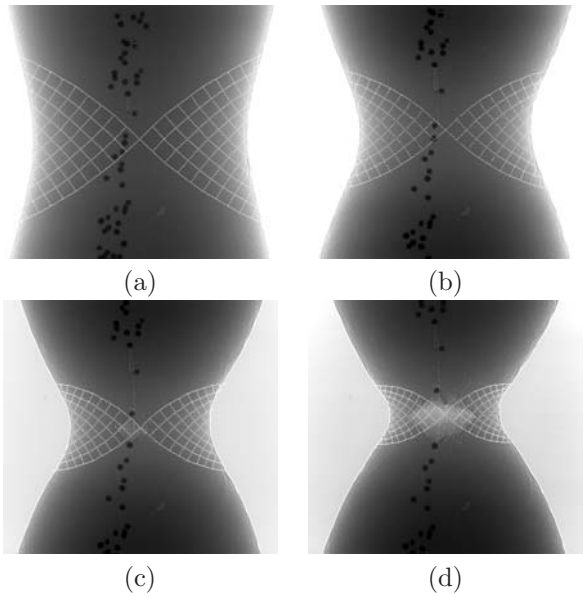

Figure 11: Slip line field representing the displacement field (or maximum shear stresses directions) in the neck of the sample.

7.2 Void coalescence in the composite core

The coalescence in the composite core occurs by a localization process acting on the voids. The localization can occur as a result of the interaction between the voids and/or as a result of the neck formation. Interaction between the voids dominate void coalescence when the volume fraction of particles is high and the effect of the neck geometry seems to dominate at low particle volume fractions. The effect of the neck geometry is seen in Figure 2 where there is only one void and its growth is therefore related to the neck geometry. When the volume fraction of particles is high, voids are nucleated at low strains and the coalescence takes place before a deep neck has time to form. In that case, the void interaction effects have more impact on void coalescence. However, it is hard to distinguish the effect of both neck geometry and voids interaction as they occur simultaneously.

7.3 Void growth after/during coalescence

In comparison to the work of Spencer et al. [13], where a single void grows through the whole width of the sheet, in our case the void growth leads to a diamond-like shaped void and the axisymmetry of the void geometry is maintained to the final failure of the sample. This shape arises from the hole growth along a typical displacement field imposed by the developing neck. This is shown by the slip line fields superimposed on the radiographs in Figure 11. This slip line field is that proposed by Hill [14] and assumes a non-hardening material. However, even though the composite materials studied here strain hardens, the work hardening rate at the strain where coalescence takes place is almost zero (see Figure 8). This is the reason why the slip line field perfectly matches the shape of the growing void. A finite element simulation has also been carried out to verify if the diamond-like shape can be predicted. Because we are interested in the void growth behavior and not in the nucleation event, the initial geometry in the model is that from the experiment at the nucleation event (between Figures 2(b) and (c)). The initial hole diameter is equal to the size of a Zirconia/Silica particle (50 μm) and the shape of the neck follows

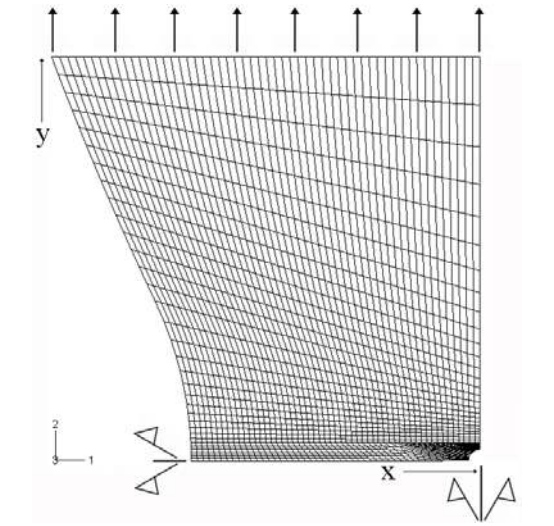

(a)

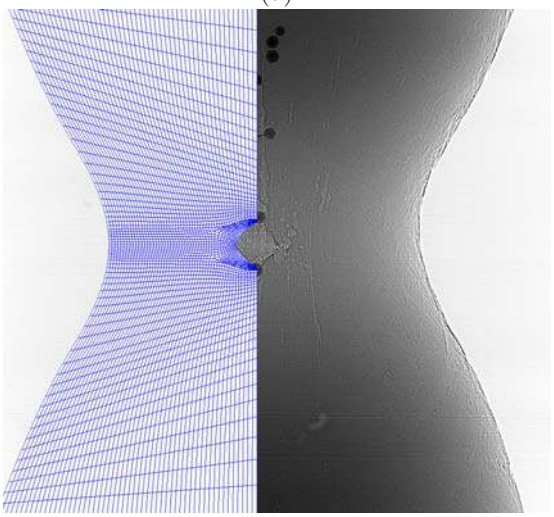

(b)

Figure 12: (a) The finite element model containing a sphere of radius equal to the radius of a Zirconia particle (25 μm). (b) Superposition of an axisymmetric finite element simulation on a radiograph of the composite containing 2% of particles in the core.

the experimental one. Only one fourth of the sample has been modelled because of the two planes of symmetry for this particular geometry. The symmetry planes are parallel to the model edges and the F.E. model represents the upper-left part of the sample. Using the coordinate system of Figure 12(a), planes with $X_1 = x$ and $X_2 = 0$ have a mirror symmetry and the curved plane has a stress free boundary condition (left hand side of FE model). The load is applied to the sample by imposing the displacement in X_2 direction of the nodes in the surface $X_2 = y$. Linear reduced-integration axisymmetric elements (CAX4R from the Abaqus library) have been used. Simulations were carried out with Abaqus/Standard [17] within the framework of the finite deformation theory with the initial unstressed state as reference. The pure aluminum matrix was modelled as an isotropic elastoplastic solid following the Von Mises criterion with isotropic hardening. The materials elastic constants were E=70 GPa and $\nu = 0.33$, and the material was assumed to be perfectly plastic with a the flow stress σ_y=200 MPa. An automatic remeshing technique (standard in Abaqus v.6.5) had to be used in order to have such large deformations without excessive distortions of the finite element mesh.

From the finite element results presented in Figure 12(b) one can see that the shape of the hole follows exactly that found experimentally and is therefore a natural consequence of the plasticity and stress state in the sample.

8 Conclusion

Metal matrix composites with a core-shell design were fabricated and tested in-situ in an x-ray tomography set-up. The core-shell design allows a controlled failure of the material because the pure aluminum shell prevents the material from failing in a stochastic manner. Samples with various volume fraction of particles in their core and different notch sizes were tested.

Both nucleation and coalescence strains can be precisely determined from the radiographs taken during the in-situ tensile test. Even though there are no significant differences in the overall failure strains for

the various samples tested, locally the results are consistent and show that the higher the volume fraction of particles in the core, the lower the nucleation and coalescence strains.

When localization (which is defined here as the onset of coalescence) proceeds, the initially ellipsoidal voids transform into diamond-like shaped voids. We demonstrated that this shape is a simple result of the plasticity in the sample being influenced by the external neck geometry.

Experiments with notched samples showed as expected a drastic decrease in the coalescence strains with a higher decrease at higher stress triaxialities.

Finally, the Brown and Embury model gives excellent predictions for the coalescence strains of the uniform samples but cannot predict those of the notched specimens. We propose a modified version of the Brown and Embury model which takes into account the variations in intervoid ligament length. The modified model is now able to predict coalescence at various stress triaxialities.

Acknowledgement

We gratefully acknowledge the support of the Natural Sciences and Engineering Research Council of Canada (NSERC), the ID19 staff for its assistance during the experiments at ESRF and Jose Ferreira for automatizing the driving motor of the tensile rig.

References

[1] P.F. Thomason, Ductile Fracture of Metals, Pergamon Press, Oxford, 1990.

[2] A. Brownrigg, W.A. Spitzig, O. Richmond, D. Teirlinck, J.D. Embury, Acta Metallurgica, 31 (1983) 1141.

[3] T. Pardoen, J.W. Hutchinson, Journal of the Mechanics and Physics of Solids, 48 (2000) 2467.

[4] J. Gammage, D.S. Wilkinson, Y. Brechet, J.D. Embury, Acta Materialia, 52 (2004) 5255.

[5] J.R. Rice, D.M. Tracey, Journal of the Mechanics and Physics of Solids, 17 (1969) 201.

[6] A.L. Gurson, Journal of Engineering Materials and Technology, 99 (1977) 2.

[7] A.A. Benzerga, Journal of the Mechanics and Physics of Solids, 50 (2002) 1331.

[8] L. Babout, E. Maire, J.-Y. Buffière, R. Fougères, Acta Materialia, 49 (2001) 2055.

[9] E. Maire, D.S. Wilkinson, J.D. Embury, H. Henein, Metallurgical Transaction A, 29 (1998) 2613.

[10] J.-Y. Buffière, E. Maire, P. Cloetens, G. Lormand, R. Fougères, Acta Materialia, 47 (1999) 1613.

[11] P.W. Bridgman, Studies in Large Plastic Flow and Fracture, New York, 1952.

[12] Le Roy, G. and Embury, J.D. and Edward, G. and Ashby, M.F., Acta Metallurgica, 29 (1981) 1509.

[13] K. Spencer, S.F. Corbin, D.J. Lloyd, Materials Science and Engineering A, 325 (2002) 394.

[14] R. Hill, The Mathematical Theory of Plasticity, London, 1950.

[15] F. Tang, I.E. Anderson, S.B. Biner, Journal of Light Metals, 2 (2002) 201.

[16] M. Brown, J.D. Embury, Third International Conference on the Strength of Metals and Alloys, Institute of Metals, London (1973) 168-164.

[17] Abaqus (2006) Users Manual, ABAQUS Inc.